Dynamical phase separation on rhythmogenic neuronal networks

Mihai Bibireata,[1] Valentin M. Slepukhin,[1] and Alex J. Levine[1,2,3]
[1]*Department of Physics and Astronomy, UCLA, Los Angeles, California 90095-1596, USA*
[2]*Department of Chemistry and Biochemistry, UCLA, Los Angeles, California 90095-1596, USA*
[3]*Department of Computational Medicine, UCLA, Los Angeles, California 90095-1596, USA*

(Received 19 January 2020; accepted 20 May 2020; published 11 June 2020)

We explore the firing-rate model of excitatory neurons with dendritic adaptation (the Feldman–Del Negro model [J. L. Feldman and C. A. Del Negro, Nat. Rev. Neurosci. **7**, 232 (2006); D. J. Schwab *et al.*, Phys. Rev. E **82**, 051911 (2010)] interacting on a fixed, directed Erdős-Rényi network. This model is applied to the dynamics of the pre-Bötzinger complex, the mammalian central pattern generator with $N \sim 10^3$ neurons, which produces a collective metronomic signal that times inspiration. In the all-to-all coupled variant of the model, there is spontaneous symmetry breaking in which some fraction of the neurons becomes stuck in a high-firing-rate state, while others become quiescent. This separation into firing and nonfiring clusters persists into more sparsely connected networks. In these sparser networks, the clustering is influenced by k cores of the underlying network. The model has a number of features of the dynamical phase diagram that violate the predictions of mean-field analysis. In particular, we observe in the simulated networks that stable oscillations do not persist in the high-sensitivity limit, in contradiction to the predictions of mean-field theory. Moreover, we observe that the oscillations in these sparse networks are remarkably robust in response to killing neurons, surviving until only approximately 20% of the network remains. This robustness is consistent with experiment.

DOI: 10.1103/PhysRevE.101.062307

I. INTRODUCTION

Networks of connected neurons, or neuronal microcircuits, play a variety of roles [1]. Their collective dynamical properties depend upon both their network structure, i.e., the pattern of which neurons are synaptically coupled to each other, and the neurons' individual properties, i.e., the relationship between input and output at the level of a single neuron. A case of particular interest is the network demonstrating regular oscillatory, or rhythmogenic, behavior that emerges from collective properties of the network rather than from the properties of single neurons. Excitation only is not enough to obtain the desired oscillations; inhibition is also required. Inhibition can be realized either by adding inhibitory neurons to the network or by introducing an internal variable for each neuron, modulating its sensitivity [2,3]. The latter approach was used to model the pre-Bötzinger complex (preBötC) [2,3], the central pattern generator establishing the inspiratory rhythm in mammals [4–6].

Specifically, the slow internal variable (identified by experiment to be dendritic calcium concentration [7]) leads to the oscillatory behavior in the following way. The calcium concentration increases with each excitatory postsynaptic potential (EPSP). In the proposed model, when the calcium concentration is below a threshold, the neurons are sensitive to external voltage signals (EPSPs) and, through mutual excitatory interactions, they collectively increase their firing rate. This collective high-firing-rate period represents the inspiratory signal. When many neurons have a high firing rate, however, the total input voltage to a typical neuron becomes sufficiently high that its dendritic calcium concentration rises above threshold, rendering that neuron insensitive to further input. As a result, the neurons' firing rate rapidly decreases and remains low until the next period of mutual excitation that occurs once the dendritic calcium concentration of a typical neuron has fallen below the threshold, restoring those neurons' sensitivity to input.

In addition to the stably oscillating phase of the network, the model was shown to admit two other phases: a quiescent phase, characterized by a steady-state low-firing rate throughout the network, and a high-activity phase, characterized by a high firing rate [3]. A dynamical phase diagram of this system was obtained as a function of network size and basal (low calcium) neuronal excitability both in a mean-field analysis and numerically on a set of Erdős-Rényi (ER) graphs [3]. Intriguingly, the numerically obtained phase boundary between the stably oscillating and high-activity phases demonstrates significant deviations from the mean-field theory predictions, with discontinuous jumps whose position on the phase diagram corresponds to the number of neurons at which the highest-k k core [8] of the network vanishes [3].

In this paper we continue to explore the rhythmogenic properties of the model. In order to understand the underlying mechanism leading to the breakdown of mean-field behavior and the emergence of k cores affecting the dynamical phase boundaries, we study broadly the phase behavior of the model over a wide parameter range that includes the current understanding of physiological preBötC. As a result, we observe a type of dynamical permutation symmetry breaking in which neurons dynamically separate into high- and low-firing-rate groups on a network that maintains the permutation symmetry of the neurons' connectivity. This dynamical symmetry breaking, i.e., spontaneous activity phase separation, is responsible both for the unexpected roughness of the phase boundaries

and for the emergence of k cores in locating the steps in those boundaries. Moreover, we observe that the dynamical phase space of the model is much richer than previously thought. In particular, we find that the region of phase space consistent with stable oscillations is bounded in both network size and neuronal basal excitability. This is inconsistent with the mean-field predictions. We analyze activity phase separation on random networks both numerically and analytically, showing that the connectivity disorder of the random networks guides the separation process. After having broadly investigated the model over a wide range of parameters, we present results for systems with the expected physiological parameters. We note that the current bonds on these physiological parameters are rather large. Consequently, we mention which of our results are robust with respect to changing those parameters. Finally, we note that the model system is remarkably robust to point (i.e., neuron) damage; this robustness is in semiquantitative agreement with experimental observations.

We organize the rest of the paper as follows. In Sec. II we demonstrate spontaneous activity separation using a small network to elucidate the process. We show how activity phase separation generates the observed roughness of the phase boundaries, a feature not captured by mean-field theory. For the special case of an all-to-all coupled network, one can analytically derive activity phase separation. We do so and compare these results to numerical simulations on all-to-all coupled networks in Sec. III. From that analysis we learn that the steepness of the neuronal firing rate function (as a function of somatic potential) controls this spontaneous symmetry breaking on the network. In Sec. IV we move to the case of more sparsely connected networks, chosen from the ensemble of ER networks, where we prove that the activity separated solution, if it exists, is stable for sufficiently sharp neuronal firing-rate functions. The cases where such activity separated solutions do not exist is reminiscent of converse symmetry breaking [9], where symmetric solutions can be paradoxically stabilized by system asymmetry.

In Sec. V we consider the role of k cores in determining which neurons fall into the high-activity state in sparsely connected networks. We prove that, when setting the low somatic voltage firing rate to zero, activity phase separation is exactly controlled by the k cores. We suggest that k cores remain relevant in controlling the phase boundary between the quiescent and high-activity phases of the disordered system, but these topological features cannot alone account for the roughness of the high-activity–stable-oscillation phase boundary.

In Sec. VI we summarize our main results on activity phase separation and discuss the implications of our analysis for the physiological preBötC. The reader primarily interested in our predictions for the *in vitro* preBötC system may choose to turn to that section. Readers interested in simulations will find a reference to our software and appropriate parameters in Appendix E.

II. THE FELDMAN–DEL NEGRO MODEL

Following Ref. [3], we describe the two-compartment neuron model of preBötC neurons. The ith neuron is characterized by two dynamical variables, its somatic potential V_i and its dendritic calcium concentration C_i. Their dynamics is controlled by the equations

$$\frac{dV_i}{dt} = \frac{1}{\tau_V}(V_{\rm eq} - V_i) + \Delta V(C_i)\sum_j M_{ij} r(V_j), \tag{1}$$

$$\frac{dC_i}{dt} = \frac{1}{\tau_C}(C_{\rm eq} - C_i) + \Delta C \sum_j M_{ij} r(V_j), \tag{2}$$

where $\Delta V(C)$ and $r(V)$ are defined by

$$\Delta V(C) = \Delta V_{\rm max}\sigma\left(\frac{C^* - C}{g_C}\right) \tag{3}$$

and

$$r(V) = (r_m - r_b)\sigma\left(\frac{V - V^*}{g_V}\right) + r_b. \tag{4}$$

In Eqs. (3) and (4) we have introduced the standard sigmoid (Fermi) function

$$\sigma(x) = \frac{1}{1 + e^{-x}}. \tag{5}$$

Here and throughout the paper we work in dimensionless calcium concentration units obtained by setting $C_{\rm eq} = 0$ and $C^* = 5$.

Equation (1) is typical of a leaky integrate and fire model for an excitatory neuron. The principal addition in the two-compartment model is dendritic adaptation, which is built into $\Delta V(C_i)$ defined in Eqs. (3) and (5). An incoming EPSP produces an increase in both dendritic calcium concentration ΔC and somatic potential $\Delta V(C)$; however, above a threshold concentration C^*, $\Delta V(C)$ becomes small, rendering the neuron insensitive to subsequent EPSPs. In the absence of incoming EPSPs, the dendritic calcium concentration returns to $C_{\rm eq}$ on a timescale of τ_C at which point the neuron is once again sensitive to EPSPs.

The parameter space of the neuron model is controlled by a small set of physiological constants. There are the steady-state dendritic calcium concentration and somatic potential $C_{\rm eq}$ and $V_{\rm eq}$, respectively. The voltage-dependent firing rate is determined by the basal and maximal firing rates r_b and r_m as well as g_V, which controls the steepness of the transitions around the threshold voltage V^*. Dendritic adaptation is parametrized by the maximum voltage increment associated with an EPSP $\Delta V_{\rm max}$, a calcium concentration threshold C^*, and a steepness parameter g_C, analogous to g_V discussed above. In addition to the two timescales $\tau_V < \tau_C$ for the relaxation of the somatic potential and dendritic calcium, there is a fixed calcium concentration increment ΔC associated with the response to an EPSP. Table I provides the currently available values of the model parameters.

The model also depends on the size and connectivity of the underlying network of synaptic connections between the neurons. The network's structure can be encoded by an adjacency matrix $\mathcal{M}$ whose matrix elements $M_{ij} = 1$ if neuron i synapses on neuron j and equal to zero otherwise. In this paper we consider only networks built from uncorrelated stochastic connections, i.e., Erdős-Rényi directed graphs [13]. An ensemble of such networks is determined by a single probability p that any nondiagonal matrix element is equal to one. We exclude the possibility of a neuron synapsing on

TABLE I. Model parameters known from experiment.

Parameter	Approximate value	Reference
V_{eq}	−65 mV	[1]
V^*	−50 mV	[1]
τ_V	20 ms	[10,11]
r_m	40 Hz	[10,11]
r_b	0.1 Hz	[11]
ΔV_{max}	2.8 mV	[10,11]
p	0.065	[10]
N	10^3	[10,12]

itself. The all-to-all network is simply the case of such an ER graph with $p = 1$.

Dynamical phase diagram

For a given set of parameters and given network of N neurons, the dynamical system evolves deterministically from a set of $2N$ initial conditions leading to a fixed point, limit cycle, or chaotic dynamics at long times. We find multiple fixed points, which can be further distinguished as quiescent, where the somatic potential averaged over the network of neurons $\langle V \rangle$ lies below the transition to the high-firing state V^*, or high activity (HA), where $\langle V \rangle > V^*$ [3]. Similarly, we can distinguish three classes of stable limit cycle oscillations: below-threshold oscillations (BTOs), where the oscillatory average voltage remains below the threshold for a high firing rate; above-threshold oscillations (ATOs), where the oscillatory average voltage remains above the threshold for a high firing rate; and true metronomic activity (TMA), where the stable limit cycle oscillations carry the system between high and low firing rates, producing the physiologically observed inspiratory rhythm. While these three oscillatory phases were not distinguished in [3], we do so here to give a more precise picture of the model's dynamical states.

To examine the dynamical phase behavior of the system, we vary the basal excitability of the neurons ΔV_{max} and the size of their network N while fixing the rest of the parameters. We study a range of network sizes $10 \leqslant N \leqslant 10^3$, using the smaller networks ($N \approx 10^2$) for their computational efficiency[1] and the larger networks ($N \approx 10^3$) to approach the size of the physiological preBötC. We find that our principal results, i.e., activity phase separation and phase boundary roughness, appear in both small networks and larger ones. In Sec. VI we return to the question of the model's large-N limit, where we demonstrate that one can explore arbitrarily-large-N networks via a scaling relation.

Typical results for dynamical phase diagrams of the networks are shown in Fig. 1 for three different choices of the fixed variables. We observe in Fig. 1(a) the numerically determined phase diagram for all-to-all coupled networks, which agrees with the mean-field solution of the model shown in Appendix C. In general, we find that the numerically determined phase diagram agrees with the mean-field approximation in all-to-all networks (for arbitrary initial conditions) as long as the transition in dendritic sensitivity is sufficiently smooth, i.e., $g_C \gtrsim 1$ (see Appendix B). In this limit we observe all five dynamical phases: quiescent [light blue (lightest

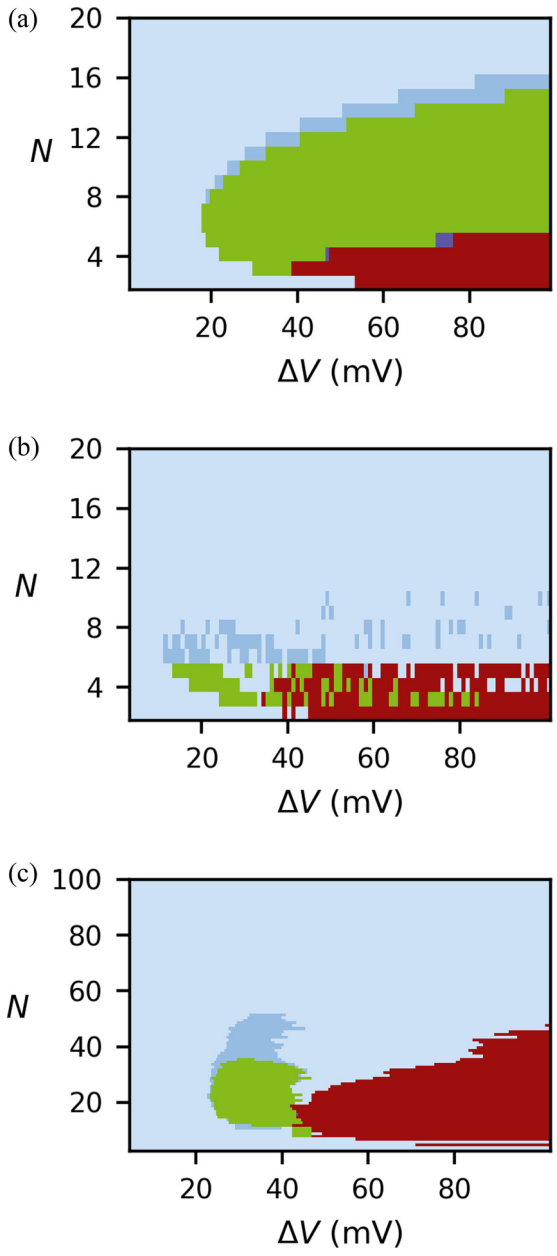

FIG. 1. Dynamical phase diagram of the model as a function of the size of the network N and basal neuronal excitability ΔV. (a) An all-to-all coupled network with large $g_C = 3$ produces phase behavior consistent with mean-field predictions, but (b) sharp sigmoid functions (small $g_C = 0.01$) produce a disordered diagram in which all dynamical phases are strongly mixed and the network dynamics is highly dependent on initial conditions. Finally, (c) randomly connected networks ($p = 0.2$) with large $g_C = 3$ have initial-condition-independent results with a modified dynamical phase diagram. In all three panels the phases are quiescent [light blue (lightest gray)], BTO [blue (light gray)], HA [dark red (darkest gray)], ATO [purple (dark gray)], and TMA [green (medium gray)]. All parameter values are listed in Appendix E.

[1]The simulation time scales as N^2 for a single network and as N^3 to map the phase diagram for a particular set of network parameters.

gray)], BTO [blue (light gray)], ATO [purple (dark gray)], TMA [green (medium gray)], and HA [dark red (darkest gray)].

There are two ways to invalidate the mean-field predictions. The first is to make the dendritic calcium adaptation more abrupt, i.e., decrease $g_C \lesssim 1$ while retaining the all-to-all coupling. In that case, we encounter a much more complex phase space as shown in Fig. 1(b), where the phases mix on a small scale in the parameter space. We also observe a dependence upon initial conditions. We discuss the quasiperiodic pattern arising in this case in Appendix D. In effect, not only is the dynamical phase diagram highly heterogeneous, but also the regions that we associate with a particular phase may depend on the choice of initial conditions. The mean-field analysis is nonpredictive, and one may say that even the introduction of a dynamical phase diagram is not as well defined as in the mean-field case.

The second way to invalidate the mean-field predictions is more interesting. We maintain the smooth neuronal sigmoid functions, but reduce the number of network connections. In that case, as shown in Fig. 1(c), the phase behavior of the network is once again insensitive to initial conditions. Moreover, the general structure of the mean-field phase diagram is preserved, but the phase boundaries are distorted. Both the HA [dark red (darkest gray)] and quiescent [light blue (lightest gray)] phases expand, while the physiologically relevant TMA (green) phase shrinks. Both the TMA and BTO [blue (light gray)] phases are now bounded, whereas they extended to arbitrarily large ΔV in the mean-field prediction. In this regime, we do not see chaotic dynamics, unlike in the cases where g_C is small. Changing other parameters of the model changes the shape of the phase boundaries, but does not introduce new dynamical phases. Both routes to the breakdown of mean-field theory (small g_C and more sparsely connected networks) are related to an inherent instability toward activity phase separation. We discuss this in more detail below.

Before discussing the phase separation, we note that the roughness of the phase diagram in the non-mean-field regime, as shown in Fig. 1(c), implies that the physiologically desirable stably oscillating phase (TMA) admits a type of reentrant behavior in which one can remove neurons (decrease N) from a network in the high-activity state to render it in the stably oscillating TMA phase. In Fig. 2 we see examples of such possible transitions at $\Delta V = 18$ mV (indicated by the vertical dashed line) where by decreasing the number of neurons from $N = 90$ to $N = 65$ one encounters TMA-HA-TMA-HA transitions, before remaining in the HA phase below $N = 72$. This suggests a specific experimental test of the fundamental model that can be made by looking for these reentrant dynamical transitions upon killing neurons in the network. In this figure we also show with black horizontal lines the values of N at which various k cores of the network vanish. The positions of the tongues of extra stability of the oscillating TMA phase appear to be bounded by these k-core transitions, suggesting that the disappearance of high-k k cores changes the stability of the oscillatory (TMA) phase. We return to this point in Sec. V, where we show that k cores play a dominant role in the phase stability of a somewhat simplified version of the model.

The fact that removing neurons from the network can enhance its ability to maintain stable oscillations seems to

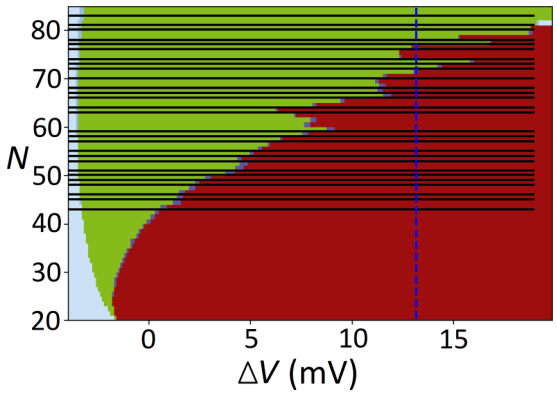

FIG. 2. Reentrant behavior along the TMA-HA phase boundary. The k-core transitions are shown as black lines, and colors are the same as in Fig. 1. All parameter values are listed in Appendix E.

be counterintuitive. This reentrant behavior appears at many phase boundaries in the system, including the one between the high-activity and quiescent phases. An example of such reentrant behavior at this phase boundary is shown in Fig. 3. To understand how this behavior emerges, it is simpler to study this case where the neurons' dynamics reaches a fixed point rather than a limit cycle. Consider a fixed point of the system; setting the time derivatives on the left-hand sides of Eqs. (1) and (2) equal to zero, we obtain

$$V_i = V_{\text{eq}} + \Delta V(C_i)\tau_V \sum_j M_{ij} r(V_j), \tag{6}$$

$$C_i = C_{\text{eq}} + \Delta C \tau_C \sum_j M_{ij} r(V_j). \tag{7}$$

For neuron i to be rapidly firing, it must receive a number of EPSPs consistent with both $V_i > V^*$ and $C_i < C^*$. In this way, its somatic voltage is maintained above the threshold and it remains sensitive to EPSPs. Too many EPSPs will drive $C_i > C^*$, resulting in the neuron's somatic potential falling

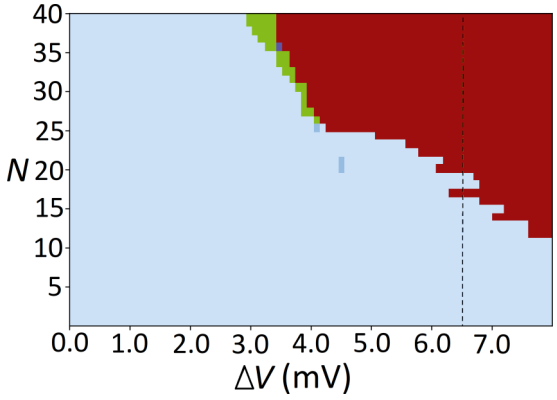

FIG. 3. Phase diagram showing reentrant behavior at the quiescent- [light blue (lightest gray)] HA [dark red (darkest gray)] phase boundary. There are also small regions of the oscillatory phases: TMA [green (medium gray)], ATO [purple (dark gray)], and BTO [blue (light gray)]. The black vertical dashed line shows the reentrant behavior. The moving along this line is shown in Fig. 4. All parameter values are listed in Appendix E.

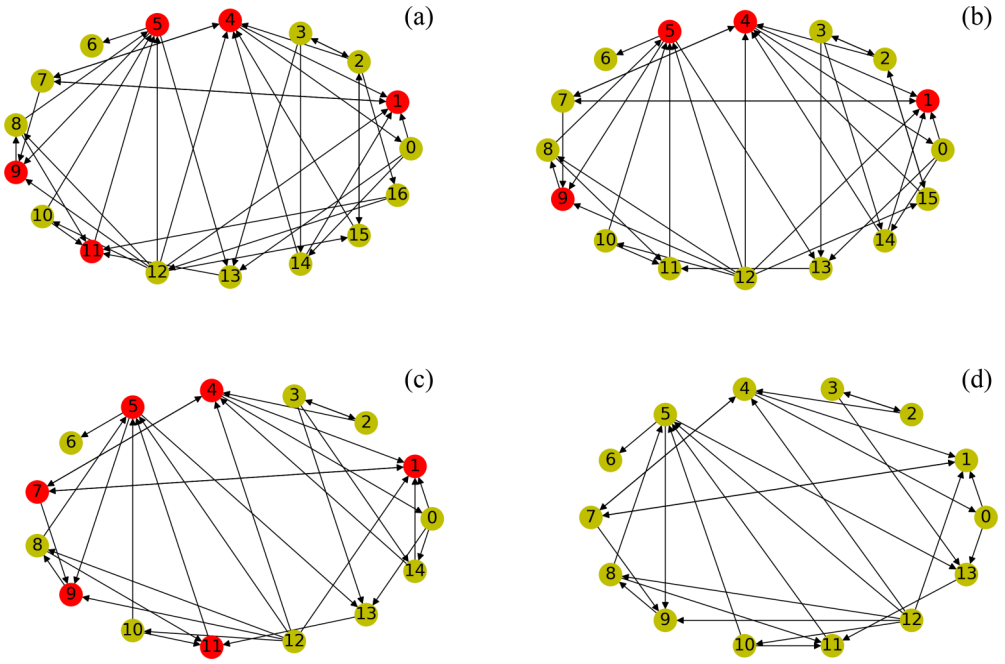

FIG. 4. Example of reentrant high activity on a small network. Red (dark gray) neurons have $V > V^*$ and dark yellow (light gray) $V < V^*$. The neurons are numbered and the last neuron in each network is removed when going from A to B to C to D. With the removal of neuron 16 (from A to B), the somatic potential of neuron 11 drops below the threshold, as it has insufficient voltage input, and the average network voltage falls below V^* too. Going from B to C, neuron 15, which synapses to neuron 4, is removed, which lowers its calcium concentration. As a consequence, the somatic potential of the neuron 4 increases as well as its firing rate, resulting in increasing the firing rate and voltage input to neuron 7. The somatic potential of neuron 7 then goes above the threshold too. The increasing firing rate of neuron 4 also raises the somatic potential of neuron 0, which raises the somatic potential of neuron 13, which in turn raises it for neuron 11. Although somatic potentials of neurons 0 and 13 do not exceed V^*, that of neuron 11 does. As a result, the average voltage of the network rises above V^*. Finally, when neuron 14 is removed (from C to D), all neurons are deactivated and ΔV must increase to restore high activity. All parameter values are listed in Appendix E.

below that threshold, while too few EPSPs will allow $V_i < V^*$ even while maintaining dendritic sensitivity. As a result, the stable configuration of $V_i > V^*$ and $C_i < C^*$ can be destroyed by either adding or removing neurons that synapse on neuron i. We can see precisely how this works in an example of a small network of 17 neurons poised near the HA-quiescent boundary.

In Fig. 4 we see that eliminating a low-firing-rate neuron (number 16) from the network causes neuron 11 to change from a high to a low firing rate. Removing an excitatory neuron has the expected behavior of reducing the total activity of the network; however, the subsequent removal of another low-firing-rate neuron (neuron 15) results in neurons 7 and 11 once again returning to high firing rate. Finally, by removing the low-firing-rate neuron 14, the entire network collapses into the quiescent state.

III. SPONTANEOUS SYMMETRY BREAKING ON ALL-TO-ALL NETWORKS

In this section we explore phase separation on all-to-all coupled networks, i.e., those having an adjacency matrix of the form $M_{ij} = 1$ for all $i \neq j$ and $M_{ii} = 0$ for all i. The steady state of the system spontaneously breaks the permutation symmetry of the neurons. To explore this symmetry breaking, we first investigate the symmetry-preserving solution, which is obtained from the pair of differential equations

$$\frac{dV}{dt} = \frac{1}{\tau_V}(V_{\rm eq} - V) + (N-1)\Delta V(C) r(V), \tag{8}$$

$$\frac{dC}{dt} = \frac{1}{\tau_C}(C_{\rm eq} - C) + (N-1)\Delta C r(V), \tag{9}$$

which results from setting $C_i = C(t)$ and $V_i = V(t)$ for all i in Eqs. (1) and (2) and using the all-to-all adjacency matrix.

We demonstrated numerically that the dynamics of the full system (1) and (2) evolves towards this permutation symmetric solution for arbitrary initial conditions if the sigmoidal functions $P(V)$ and $\Delta V(C)$ are smooth enough [see Figs. 5(c) and 5(d)]. If, on the other hand, these sigmoid functions are sharper, the system becomes unstable towards activity phase separation (breaking the original permutation symmetry of the underlying network) into time-independent subnetworks of high- and low-firing-rate neurons, when the initial conditions are not themselves identical across the network [see Figs. 5(a) and 5(b)]. The phenomenon of activity phase separation in all-to-all biological networks has been observed in a model of cell regulatory networks [14,15].

The symmetry-broken state is of course not captured by the mean-field analysis. To explore it, we need to analyze the full system of equations. Defining the sum of firing rates over

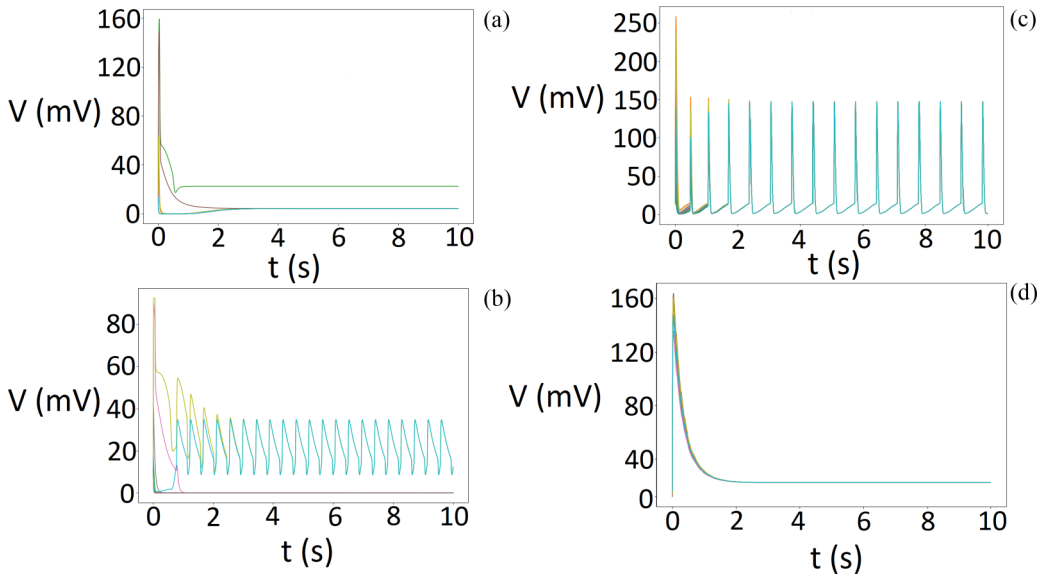

FIG. 5. Activity phase separation on an all-to-all connected network of $N = 10$ neurons. The traces show the somatic potential of individual neurons as a function of time. (a) One neuron is at high voltage, nine are quiescent, $g_V = 0.3$ mV, and $g_C = 0.5$. (b) Two neurons oscillate, eight are quiescent, $g_V = 0.3$ mV, and $g_C = 0.5$. (c) Synchronous oscillations of all neurons, $g_V = 0.1$ mV, and $g_C = 1.1$. (d) All neurons at high voltage, $g_V = 1.8$ mV, and $g_C = 10.8$. All parameter values are listed in Appendix E.

the entire network as $R = \sum_i r(V_i)$, we rewrite the dynamical system as

$$\frac{dV_i}{dt} = \frac{1}{\tau_V}(V_{\rm eq} - V_i) + \Delta V(C_i)[R - r(V_i)], \tag{10}$$

$$\frac{dC_i}{dt} = \frac{1}{\tau_C}(C_{\rm eq} - C_i) + \Delta C[R - r(V_i)]. \tag{11}$$

Now we can look for a self-consistent solution of this system, i.e., we find $V_i(R)$ such that $R = \sum_i r(V_i)$. Studying the nullclines of Eqs. (10) and (11), we see that it can have one to three fixed points. The cases of one and three fixed points are shown in Fig. 6, where we see the intersections of the nullclines of Eqs. (10) and (11) in orange (light gray) and blue (dark gray), respectively.

Since we are looking for a self-consistent solution, we cannot analyze its stability directly from the graph; however, we can find the fixed points and later analyze their stability. For neuronal parameters consistent with smooth sigmoid functions, there is only one fixed point (V_f, C_f) for a fixed value of R. This self-consistent solution is both permutation symmetric and consistent with our mean-field prediction. In contrast, for sharp sigmoid functions, there is more than one fixed point, so it is possible to find some fraction of the network neurons at a high-voltage fixed point, while the remainder is at a low-voltage fixed point. The number of neurons in these two categories is determined by the condition $R = \sum_i r(V_i)$. There is also a range of parameters with $g_V > 0$ and $g_C = 0$ such that the self-consistent solution does not exist. Therefore, there is no fixed point and only oscillations are allowed. See Appendix D for the details of the analytical calculation.

For the small values of g_C (sharp sigmoid function), the phase separation into firing and quiescent neurons is the only stable state. For intermediate values of g_C we still observe this stable state shown in Fig. 5(a). We also show activity separation into oscillating and quiescent subnetworks in Fig. 5(b). Continuing to increase g_C, we obtain synchronous oscillations of the whole network in Fig. 5(c) and finally a fixed point with constant uniform activity in Fig. 5(d).

For the case of the large physiological-like network of $N = 1000$ neurons we also observe phase separation in the case of the sharp sigmoid function (Fig. 7), which demonstrates that the separation is not the finite-size effect.

Step-function limit: All-to-all networks

To better understand activity phase separation on the network, it is useful to consider a nonphysiological limit of the model in which the sigmoidal functions describing both the firing rate and the dendritic adaptation are taken to be infinitely sharp, i.e., step functions $g_V = g_C = 0$. In this case, neurons with above-threshold voltage V^* fire at the maximal rate r_m, while neurons below that threshold voltage fire at the basal rate r_b. If the number of high- and low-firing-rate neurons are n_h and n_l, respectively $(n_h + n_l = N)$, we find that

$$V_h = V_{\rm eq} + \Delta V(C_h)\tau_V[(n_h - 1)r_m + n_l r_b], \tag{12}$$

$$C_h = C_{\rm eq} + \Delta C\tau_C[(n_h - 1)r_m + n_l r_b]. \tag{13}$$

Similarly, the low-firing-rate neurons have

$$V_l = V_{\rm eq} + \Delta V(C_l)\tau_V[(n_l - 1)r_b + n_h r_m], \tag{14}$$

$$C_l = C_{\rm eq} + \Delta C\tau_C[(n_l - 1)r_b + n_h r_m]. \tag{15}$$

One can check that the rate of spikes received by a high-firing-rate neuron $R_{\rm high} = [(n_h - 1)r_m + n_l r_b]$ is less than that received by a low-firing-rate neuron $R_{\rm low} = [(n_l - 1)r_b + n_h r_m]$. However, the condition for being at a high firing rate is $V^* < V_h$ and a low firing rate is $V^* > V_l$. For these

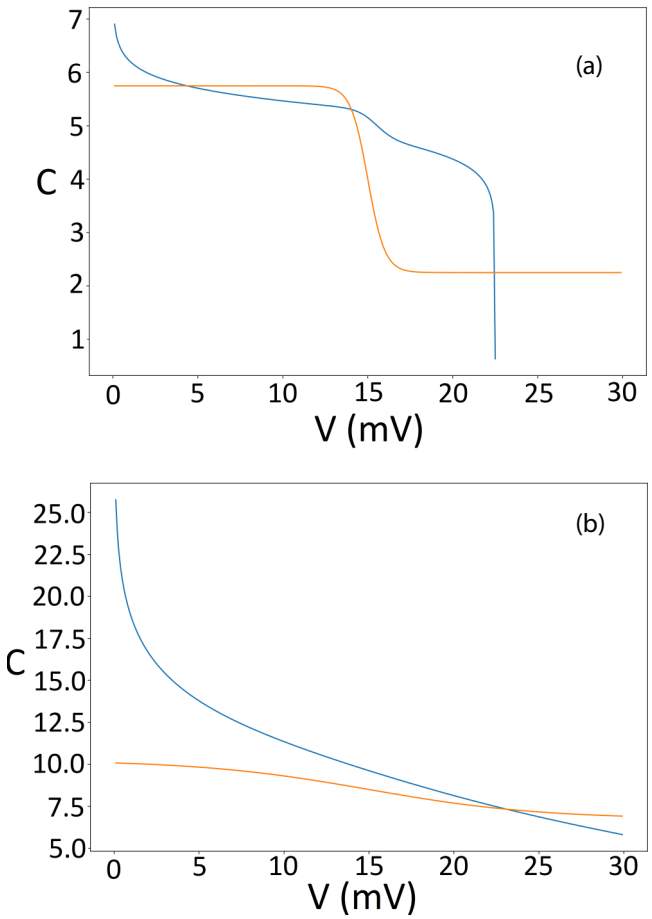

FIG. 6. Nullclines of the all-to-all $N = 10$ network described by Eqs. (10) [orange (light gray)] and (11) [blue (dark gray)]. There are either three fixed points or one fixed point, depending on the parameters. Assuming R is constant (and not fixed self-consistently), two of the fixed points annihilate in a standard pitchfork bifurcation [16]. (a) Three fixed points, $g_V = 0.5$ mV, and $g_C = 0.3$. (b) One fixed point, $g_V = 5$ mV, and $g_C = 3$. All parameter values are listed in Appendix E.

inequalities to hold simultaneously with the result that $R_{\text{high}} < R_{\text{low}}$, one needs the high-firing-rate neurons to be more sensitive to incoming spikes than the low-firing-rate ones. Thus we conclude that this state requires $C_l > C^* > C_h$. From this conclusion we find n_l, the number of low-firing-rate neurons, to be

$$n_l = \left\lfloor \frac{(Nr_m - r_b)\Delta C\tau_C + C_{eq} - C^*}{\Delta C\tau_C(r_m - r_b)} \right\rfloor, \tag{16}$$

where we have introduced the floor function: $\lfloor x \rfloor$ is equal to the integer part of the real number x.

To observe the phase-separated state, we require that the high-firing-rate neurons remain sufficiently sensitive to incoming spikes. The lower bound of their sensitivity $\Delta V(C_h)$ is given by

$$V^* - V_{\text{eq}} < \Delta V(C_h)\tau_V[(n_h - 1)r_m + n_l r_b]. \tag{17}$$

While the number of neurons at low-firing-rate neurons n_l is fixed by Eq. (16), the identity of these neurons is determined solely by the initial conditions on the all-to-all network. There is a large number $\frac{n!}{n_l!n_h!}$ of otherwise identical fixed points that are related by permutation symmetry of the network. If, however, the network is more sparsely connected and thus does not have this permutation symmetry, there are fewer fixed points, as is discussed in the following section.

IV. SYMMETRY BREAKING ON SPARSE NETWORKS

If we randomly remove edges from the all-to-all network, we break the permutation symmetry of the neurons and produce an instance of a network selected from an ensemble of ER networks with probability $p < 1$ of a directed connection between neurons. This leads to a rapid reduction in the number of stable fixed points with decreasing p, as shown in Fig. 8.

Below $p \approx 0.9$ the number of stable fixed points drops to just one or vanishes entirely, resulting in only an oscillatory or approximately chaotic solution. For the case of the step-function neurons, or for sufficiently sharp sigmoidal responses, we do not typically observe globally synchronized oscillations. The asynchronous firing of different neurons results in many self-crossing for the network averaged V vs C graph, as shown in Fig. 9.

While for the smooth sigmoid functions the most common case when oscillations occur is an unstable fixed point, this is not possible when sigmoid functions are very sharp. Indeed, any fixed point not exactly on the threshold in this case is stable, as shown in Appendix C. Therefore, the only opportunity for the oscillatory or approximately chaotic behavior is the absence of a fixed point.

Oscillations on star networks

In order to understand how all fixed points vanish in sparser networks, we consider the special case of a star network, in which one central neuron is bidirectionally coupled to $N - 1$ other neurons. Those other neurons are not coupled to each other. Such a network is shown in Fig. 10.

We choose parameters such that the range of the central neuron's firing rate is large enough to take the peripheral neurons across their firing-rate threshold:

$$\Delta V(0)\tau_V r_b < V^* < \Delta V(0)\tau_V r_m. \tag{18}$$

Furthermore, we require that all the peripheral neurons firing together at their basal rate are able to excite the central neuron over the threshold. If, however, the central neuron's dendritic calcium is above threshold, then all the peripheral neurons firing at their maximal rate are collectively insufficient to excite the central neuron:

$$(N-1)\Delta V(C > C^*)\tau_V r_m < V^* < (N-1)\Delta V(0)\tau_V r_b. \tag{19}$$

We also demand two conditions on the calcium threshold. First, a single neuron cannot fire rapidly enough to push another neuron's dendritic calcium over the threshold:

$$C^* > \Delta C\tau_C r_m. \tag{20}$$

However, $N - 1$ neurons firing at their maximal rate can induce calcium concentrations over threshold in the central neuron,

$$(N-1)\Delta C\tau_C r_b < C^* < (N-1)\Delta C\tau_C r_m, \tag{21}$$

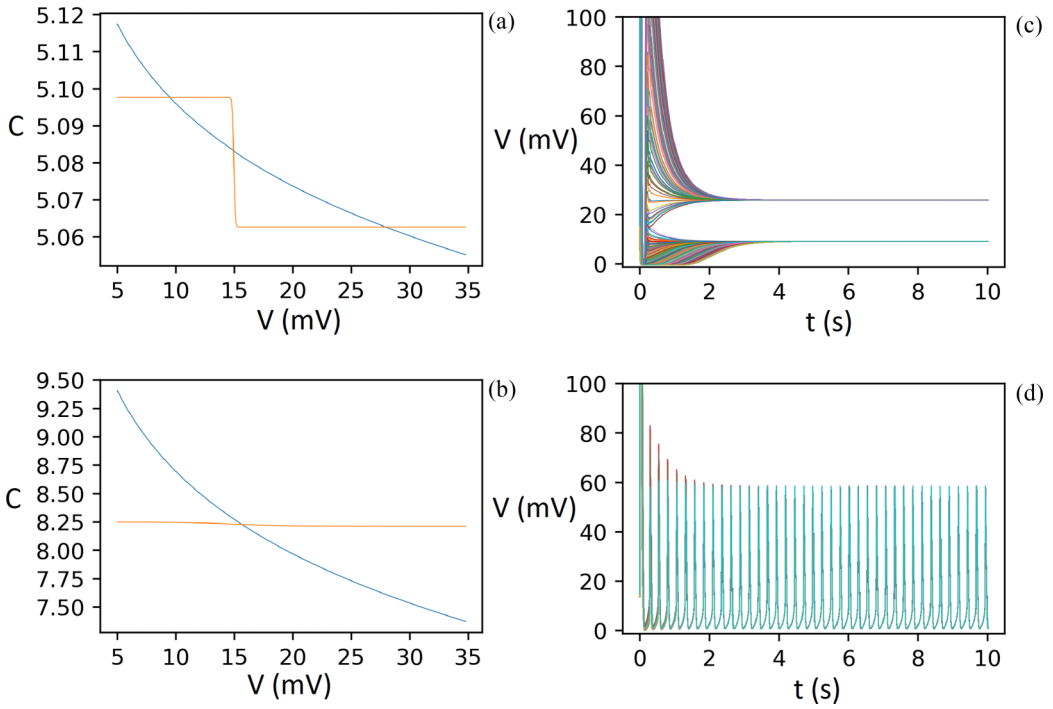

FIG. 7. Activity phase separation on an all-to-all connected network of $N = 1000$ neurons: (a) and (b) nullclines as in Fig. 6; (c) and (d) corresponding traces of voltage versus time, as in Fig. 5. (a) and (c) Activity separation is shown for $g_V = 0.05$ mV and $g_C = 0.03$. (b) and (d) No such phase separation, but synchronous oscillation is shown with $g_V = 2$ mV and $g_C = 1$. All parameter values are listed in Appendix E.

but they cannot do so when they are all firing at their basal rate.

By obeying all of the above inequalities, the system cannot reach a fixed point. Instead, the network with these step-function neurons oscillates. The central neuron excites the peripheral ones and then those neurons drive the central neuron's calcium concentration above threshold, rendering it insensitive. As a result, the central neuron returns to its low firing state and then so do the peripheral ones. At this point, the cycle begins again.

Recall, however, that the step-function neurons on the all-to-all coupled network do not oscillate; instead they reach one of many fixed points characterized by activity phase separation. By breaking the permutation symmetry of the network, the star network admits a new synchronous oscillatory phase. This is reminiscent of an effect called converse symmetry breaking [9], where the necessary condition for synchronous activity of a coupled network of oscillators is an asymmetry of this system. We observe a similar stability of globally synchronous oscillations in random networks that break the permutation symmetry such as the ER graphs discussed above.

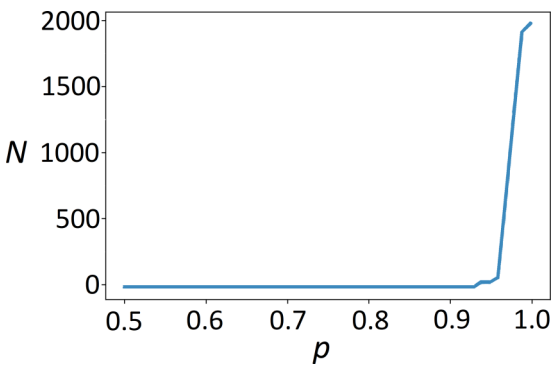

FIG. 8. Number of stable fixed points as a function of the network connectivity probability p for $N = 100$ neurons. For $p = 1$ this number coincides with $\frac{n!}{n_l!n_h!}$ and rapidly falls to one or zero when $p \lesssim 0.9$. All parameter values are listed in Appendix E.

V. EFFECT OF NETWORK HETEROGENEITY ON PHASE SEPARATION

We have established that the neuron model leads generically to activity phase separation. On permutation symmetric all-to-all networks, this phase separation is a form of spontaneously broken symmetry, but it exists on more sparse networks too. This poses the following question: How does the network topology modify phase separation? To address this, we consider another simplified limit of the model by setting $r_b = 0$ (i.e., a neuron is either firing or not), using a step-function firing rate ($g_V \to 0$), and eliminating dendritic adaptation by taking $C^* \to \infty$. The system in this limit is equivalent to the coarse-grained neuronal network considered in [17] that was based on the mutualistic ecosystem network studied in [18]. It was shown that in such a model the k core exactly coincides with the most stable part of the system (the active voxels in a subliminal state in [17] and surviving species in [18]). We repeat below the derivation of this effect in terms of the system at hand based on [17,18], demonstrating

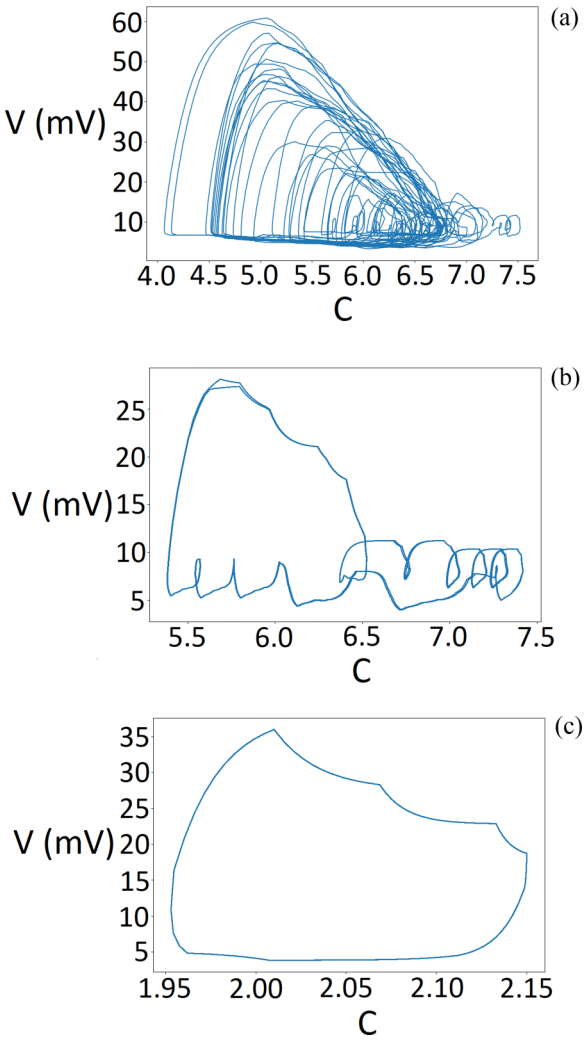

FIG. 9. Phase trajectories in the averaged V-C plane for networks with step-function neurons. (a) Almost chaotic behavior. True chaos is not observed since the number of possible states is finite, but the voltage varies wildly. (b) Limit cycle with self-intersections, indicating asynchronous firing. (c) Standard limit cycle with synchronous firing, corresponding to true metronomic activity, rarely observed in the step-function limit.

that, in this case, the cluster of firing neurons will be a k core of the network with k determined by neuronal parameters.

Consider n_i actively firing input neurons synapsing on neuron i. From the fixed-point condition $\dot{V}_i = 0$ we find

$$\frac{V_i}{\tau_V} = n_i \Delta V r_m. \tag{22}$$

For the ith neuron to be part of the group of actively firing ones, $V_i > V^*$, which implies that the number n_i of firing inputs exceeds a lower bound

$$n_i \geqslant \frac{V^*}{\tau_V \Delta V r_{\max}}. \tag{23}$$

We intend to relate the actively firing group with a topological feature of the network: a k core. This structure is defined to be the maximal subnetwork such that within it each neuron has k or more inputs from the other neurons in that

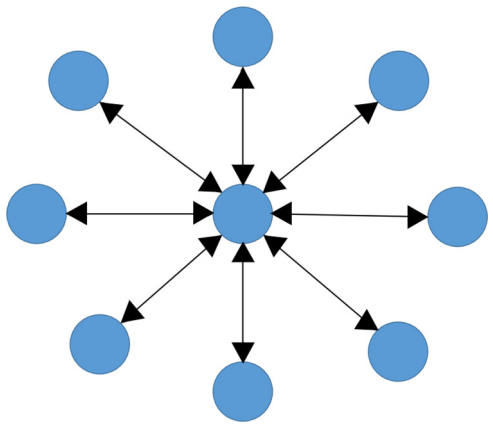

FIG. 10. Star network with $N = 9$ neurons. The peripheral neurons are bidirectionally coupled to the central neuron, but not to each other.

subnetwork. The k cores have been discussed in a variety of applications in neuroscience, bioinformatics, ecology, and the study of social networks [18–21]. The condition for a neuron to be in the actively firing group [Eq. (23)] is equivalent to membership within a k core with the integer k given by

$$k = \left\lfloor \frac{V^*}{\tau_V \Delta V r_{\max}} \right\rfloor. \tag{24}$$

If a k core with some k given by Eq. (24) is absent from the network, the dynamical system on that network relaxes to the quiescent fixed point, but if such a k core is present, the neurons making up the k core become fixed in the HA phase. We note that for typical values of k, most of the network will be part of that k core [8] because for $k > 2$ the probability of a neuron being part of the k core has a discontinuous jump from zero to a significant value as a function of the density of synaptic connections (in the thermodynamic limit of large networks).

We compare our predicted phase boundary of the system and k cores in Fig. 11. The predicted k value for a particular set of n and ΔV parameters corresponds exactly to the point in phase space where the HA phase gives way to the quiescent phase. For this restricted version of the Feldman–Del Negro model, at least, there is a precise correspondence between the neuronal network's dynamical phase behavior and the prediction made purely from the topology of the underlying network. The k cores completely determine the dynamical phase transition of the neurons interacting on them and how the network phase separates into groups of high- and low-activity neurons.

VI. DISCUSSION AND APPLICATIONS TO THE PRE-BÖTZINGER COMPLEX

We have explored the Feldman–Del Negro model of oscillations in the preBötC and found a form of dynamical phase separation on the network in which groups of neurons separate into high- and low-firing-rate fixed points. This firing-quiescent phase separation plays a crucial role in the termination of the TMA phase. One feature that emerges from this work is that the permutation-symmetric system (the all-to-all

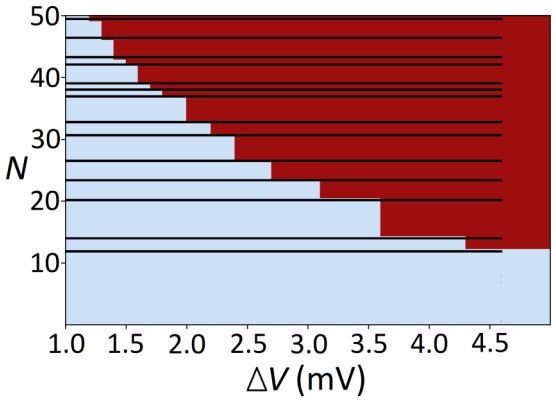

FIG. 11. Phase diagram for the simplified model discussed in Sec. V. There is no oscillatory phase, only quiescent [light blue (lightest gray)] and HA [dark red (darkest gray)]. Black horizontal lines correspond to k-core transitions. We see an almost exact correspondence between k-core transitions and steps on the phase boundary. Small deviations are due to the fact that the average voltage of the whole network can be below V^* even in the presence of the active k core due to the averaging over all neurons including quiescent ones. All parameter values are listed in Appendix E.

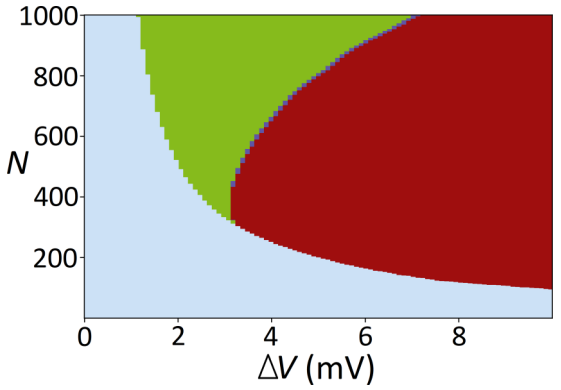

FIG. 12. Phase diagram of the network with physiologically relevant parameters. It shows three stable dynamical phases: true metronomic activity [green (medium gray)] consistent with the preBöC physiological dynamics, as well as a HA regime [dark red (darkest gray)] and a quiescent regime [light blue (lightest gray)]. There is a narrow band of above-threshold oscillations [purple (dark gray)]. The diagram corresponds to the part of the phase diagram in Fig. 13 in the black frame under rescaling, and thus does not have all the possible phases present. All parameter values are listed in Appendix E.

coupled network) admits a type of spontaneous symmetry breaking into these high- and low-activity phases. In more sparse networks such as in the physiological preBötC, this permutation symmetry is broken by the network. The details of network connectivity modify the inherent instability of the system toward phase separation into groups of high- and low-firing-rate neurons. In one particular limit of the model, we found that this interaction of neuronal dynamics and network topology is particularly simple. By examining only the k-core structure of the network, one can precisely predict both the dynamical phase diagram and which neurons will end up in the high- and low-firing-rate groups.

In the full model, the effect of the k cores in determining the phase boundaries of the dynamical system remains, but no longer does it completely control these dynamics. The incomplete influence of k cores was observed earlier [3]. Here we believe we have better elucidated the underlying mechanism and explained why their control of the dynamics is not complete.

To assess the importance of these observations for the physiological preBötC, we first present the numerically computed phase diagram for 1000 neurons using parameters consistent with physiological measurements. This is shown in Fig. 12. See Appendix A for a discussion of how the neuronal and network parameters were selected.

As discussed in Appendix A, there is a remaining uncertainty in determining the value of ΔC. Moreover, the full preBötC is somewhere between two to three times as many neurons as used in the simulation. We note, however, a scaling argument, based on the mean-field analysis of the model, that allows us to shift ΔC as a way of effectively changing the network's size. In the mean-field theory, three parameters ΔC, ΔV, and pN appear in only two combinations $pN\Delta V$ and $pN\Delta C$. As a result, if we change $\Delta C \to \frac{\Delta C}{\lambda}$, $\Delta V \to \frac{\Delta V}{\lambda}$, and $pN \to pN\lambda$ the mean-field solutions are invariant. We can test this scaling hypothesis in the full model by comparing the phase diagram of the $N = 1000$ network with $\Delta C = 2.5 \times 10^{-2}$, shown in Fig. 13, to a much smaller network of $N = 100$ and $\Delta C = 0.1$, shown in Fig. 1(c). Their correspondence supports our exploration of larger networks using calcium scaling.

The scaling hypothesis suggests that if we were able to expand the network size used in Fig. 12 to the preBötC's true physiological size, we would find that the region of stable oscillations is bounded from above as well as for high and low neuronal excitability. We see in Fig. 13 that the large-N network has a rough phase boundary between the TMA and

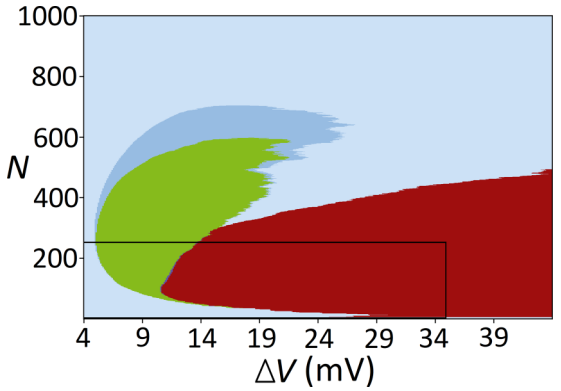

FIG. 13. Phase diagram of large networks with N up to 1000. All five phases are present: TMA [green (medium gray)], BTO [blue (light gray)], ATO [purple (darker gray)], HA [dark red (darkest gray)], and quiescent [light blue (lightest gray)]. The right TMA-BTO and BTO-quiescent boundaries demonstrate the reentrant behavior. In general, the pattern is approximately the same as in Fig. 1(c), supporting the scaling argument. The black frame shows the part of the diagram that maps onto the phase diagram in Fig. 12 under rescaling. All parameter values are listed in Appendix E.

quiescent phases on the right side of the bounded TMA domain, which is incompatible with the mean-field analysis and reflects the role of dynamical phase separation on the network. This result makes an interesting prediction in that there are regions of the phase diagram in the physiological system where *increasing* neuronal excitability can actually produce globally quiescent networks, through calcium inhibition. This feature cannot be reproduced by the mean-field model.

Another consequence of this large-N phase diagram is that we can predict the robustness of the network to damage. From Fig. 13 we see that under optimal conditions, one can destroy about 80% of the network before causing the collapse of the oscillating phase. This agrees with experimental observations [12]. One may notice that the crucial condition for this robustness is the smoothness of the sigmoid functions. If we make sigmoid functions sharper, the system becomes highly sensitive not only to damage but also to the initial conditions (see Appendix B for the influence of parameters g_V and g_C controlling the sharpness of sigmoid functions).

We propose three types of experimental tests of the above analysis. The first of these, alluded to above, is that the network should be able to be silenced by increasing neuronal excitability. Second we predict that the roughness of the phase boundaries, particularly when N is large, suggests the presence of multiple reentrant transitions in which the network goes from being oscillatory to quiescent, and back to oscillatory as neurons are removed from it. Third, one should be able to directly observe dynamical phase separation in the system. In either the high activity or quiescent phase, one should be able to find neurons trapped at the other fixed point so that the globally quiescent state of the network should harbor some fixed fraction of high-firing-rate neurons. Conversely, the network in its globally highly active state should contain a subpopulation of neurons trapped in their low-firing-rate state.

ACKNOWLEDGMENTS

A.J.L. and V.M.S. acknowledge partial support from NSF DMR Grant No. 1709785. V.M.S. acknowledges support from Peccei-Holmes Graduate Research Fellowship and the Bhaumik Institute for Theoretical Physics. A.J.L., V.M.S., and M.B. are thankful to Jack Feldman, Robijn Bruinsma, and Sufyan Ashhad for fruitful discussions.

APPENDIX A: DETERMINING PHYSIOLOGICAL PARAMETERS FOR THE MODEL

To prepare Fig. 12 we must address the current understanding of the physiological parameters of the neurons as well as the network connectivity parameters. Most of them can be fixed using the experimental data shown in Table I. (To obtain value for p from [10] we use the fact that out of 23 pairs of neurons, three were unidirectionally connected, which gives $3/23$ probability for the connection in any of two directions and half as much for the connection in the particular direction.) The exception is the set of parameters related to the dendritic calcium concentration, which are not currently as well known. We chose them to reproduce the observed dynamics of the system.

Specifically, we set τ_C to reproduce the observed period of stable oscillation. Taking into account that, for us, the units for the calcium concentration are arbitrary as is the choice of the zero for that concentration, we are left with only two independent parameters: g_C and ΔC. Here g_C is chosen to be large enough that we have reproducible phase behavior, avoiding highly heterogeneous and initial-condition-dependent results as shown in Fig. 1(b). We also require it to be small enough to produce a true threshold for calcium inactivation of the dendrite, i.e., $\frac{C_{eq}-C^*}{g_C} > 1$. The last parameter to be fixed is ΔC. The proper choice of ΔC is facilitated by the scaling behavior observed in the mean-field approximation of the model.

Indeed, consider Fig. 1(c). To quantitatively fit the *in vitro* data, the network must support stable oscillations when $\Delta V \approx 2.8$ mV, which is the average magnitude of an EPSP [10]. To do that, we choose $\Delta C = 0.007$ and find, with no remaining fitting parameters, that stable oscillations occur for networks of $N \approx 10^3$ neurons (see Fig. 12). It is computationally difficult to study networks with $N > 2000$, but we can use the rescaling property, observed in the mean-field approximation, to qualitatively predict the behavior for larger N. If we choose $\Delta C = 0.025$ and $p = 0.083$, we obtain the phase diagram, shown in Fig. 13. The result is quite similar to that shown in Fig. 1(c), which describes a much smaller system.

APPENDIX B: MEAN-FIELD SOLUTION

The mean-field solution is obtained by assuming that somatic potentials and dendritic calcium concentrations of all the neurons are the same: $V_i = V$ and $C_i = C$. Another assumption is that the network is on average homogeneously connected, i.e., each neuron on average has pN inputs and outputs, with N the total number of neurons and p the connection probability. Then Eqs. (1) and (2) are rewritten as a pair of equations for V and C,

$$\frac{dV}{dt} = \frac{1}{\tau_V}(V_{\rm eq} - V) + \Delta V(C)p(N-1)r(V), \quad \text{(B1)}$$

$$\frac{dC}{dt} = \frac{1}{\tau_C}(C_{\rm eq} - C) + \Delta C p(N-1)r(V). \quad \text{(B2)}$$

The phase diagram for such a system is shown in Fig. 14(b). One may see that it is identical to the phase diagram for the all-to-all coupled network in Fig. 14(a) in the case of a smooth transition in dendritic sensitivity. The mean-field approximation is valid for large g_V and g_C but breaks down when they become smaller. More detailed results are shown in Fig. 15.

APPENDIX C: STABILITY OF FIXED POINTS ON SPARSE NETWORKS

For the smooth sigmoid neurons, we found in Sec. III that there was only a single fixed point (see Fig. 6). When that fixed point is unstable, the system executes limit cycle oscillations. To determine the parameter range of these oscillations, here we investigate the stability of that fixed point. Expanding the equations of motion near the fixed point $\{V_i^f, C_i^f\}$ in the

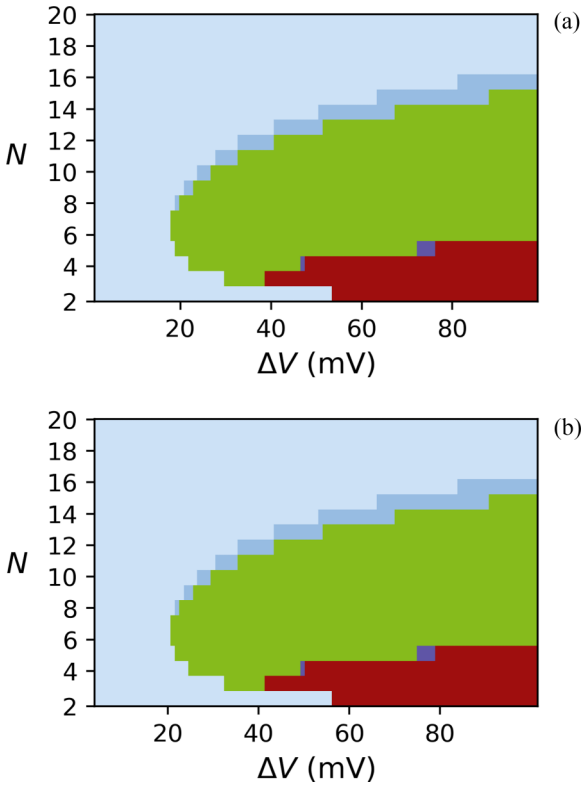

FIG. 14. (a) Phase diagram for the all-to-all coupled network, using arbitrary initial conditions and smooth sigmoid functions. It is identical to (b) the mean-field phase diagram. Phases are quiescent [light blue (lightest gray)], BTO [blue (light gray)], HA [dark red (darkest gray)], ATO [purple (dark gray)], and TMA [green (medium gray)]. All parameter values are listed in Appendix E.

$2N$-dimensional space of V_i and C_i, we define $v_i = V_i - V_i^f$ and $c_i = C_i - C_i^f$ and obtain

$$\frac{dv_i}{dt} = -\frac{v_i}{\tau_V} + \Delta V'\left(C_i^f\right)c_i \sum_j M_{ij} r\left(V_j^f\right) + \Delta V\left(C_i^f\right) \sum_j M_{ij} r'\left(V_j^f\right) v_j, \tag{C1}$$

$$\frac{dc_i}{dt} = -\frac{c_i}{\tau_C} + \Delta C \sum_j M_{ij} r'\left(V_j^f\right) v_j. \tag{C2}$$

Using $r(V)$ and $\Delta V(C)$ from Eqs. (3) and (4), we find

$$\frac{dv_i}{dt} = -\frac{v_i}{\tau_V} - \frac{1}{g_C}\Delta V_{\max}\sigma'\left(\frac{C^* - C_i^f}{g_C}\right)c_i \sum_j M_{ij} r\left(V_j^f\right) + \frac{1}{g_V}(r_m - r_b)\Delta V\left(C_i^f\right) \sum_j M_{ij}\sigma'\left(\frac{V_j^f - V^*}{g_V}\right)v_j \tag{C3}$$

and

$$\frac{dc_i}{dt} = -\frac{c_i}{\tau_C} + \Delta C(r_m - r_b) \sum_j M_{ij}\sigma'\left(\frac{V_j^f - V^*}{g_V}\right)v_j. \tag{C4}$$

Dynamical phase separation requires that neither $C^* - C_i^f$ nor $V^* - V_i^f$ vanishes. Therefore, if g_V and g_C are small, the

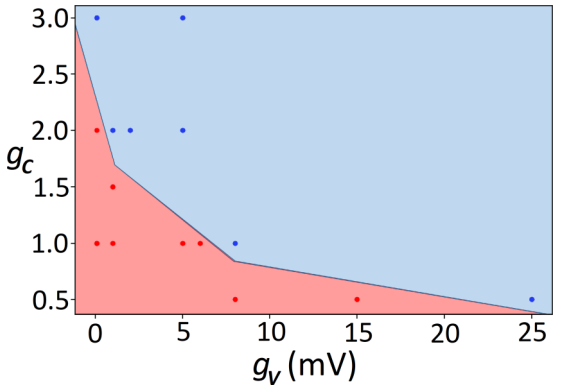

FIG. 15. Results of the simulations for different g_V and g_C. Blue (light) region [red (dark) region] points correspond to the case where the dynamics agree (disagree) with mean-field predictions, as determined by a visual inspection of the numerically obtained phase diagrams. The blue region exhibits both insensitivity to initial conditions and robustness in the face of damage. Conversely, the red region is highly sensitive to both the initial condition and damage. All parameter values are listed in Appendix E.

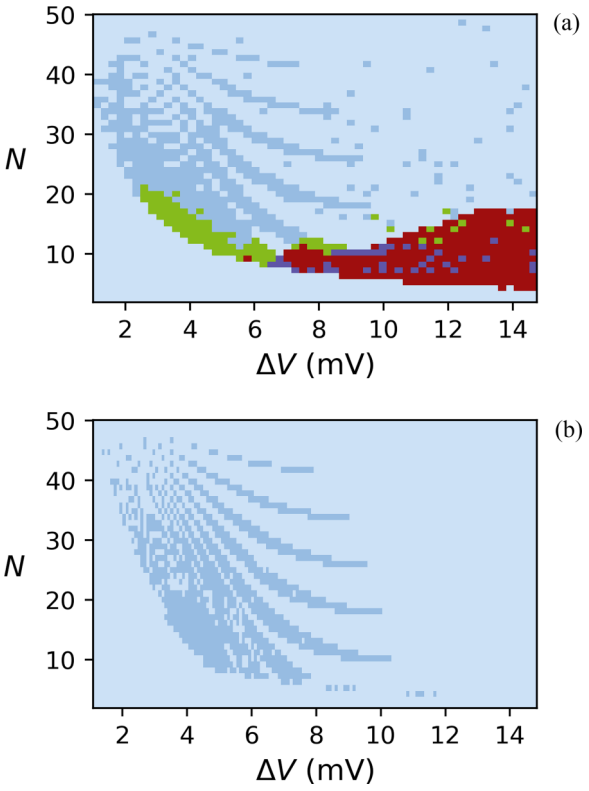

FIG. 16. (a) Phase diagram for the all-to-all coupled network, with $g_C = 0$ and $g_V > 0$. All five previously mentioned phases are present. There is a quasiperiodic pattern on the BTO- [blue (light gray)] quiescent [light blue (lightest gray)] boundary. This phase diagram fits (b) the theoretical prediction where blue (lightest gray) corresponds to the case that Eq. (D6) has a solution and dark red (darkest gray) to the case that it does not. All parameter values are listed in Appendix E.

TABLE II. Parameters used in the simulation.

Figure	g_C	g_V (mV)	C^*	$V^* - V_{\rm eq}$ (mV)	τ_C (ms)	τ_V (ms)	r_m (Hz)	r_b (Hz)	ΔC	$\Delta V_{\rm max}$ (mV)	p	N
1(a)	3	5	5	15	500	10	75	5	0.1	0–100	1	2–20
1(b)	0.01	5	5	15	500	10	75	5	0.1	0–100	1	2–20
1(c)	3	5	5	15	500	10	75	5	0.1	0–100	0.2	2–100
2	5	5	15	15	500	10	75	5	0.035	0–25	0.75	2–100
3	0	0	15	15	500	10	75	5	0.1	5–30	0.5	2–20
4	0	0	15	15	500	10	75	5	0.1	10	0.5	6–9
6(a)	0.3	0.5	5	15	500	10	75	5	0.1	50	1	10
6(b)	3	5	5	15	500	10	75	5	0.1	50	1	10
5(a)	0.3	0.5	5	15	500	10	75	5	0.1	50	1	10
5(b)	0.3	0.5	5	15	500	10	75	5	0.1	50	1	10
5(c)	1.1	0.1	5	15	500	10	75	5	0.1	50	1	10
5(d)	10.8	1.8	5	15	500	10	75	5	0.1	50	1	10
7(a),7(c)	0.03	0.05	5	15	500	10	75	5	0.001	2.5	1	1000
7(b),7(d)	1.0	2.0	5	15	500	10	75	5	0.001	2.5	1	1000
8	0	0	20	15	500	10	70	5	0.015	7.3	0.5–1	100
11	0	0	∞	15	500	10	70	5	0.1	1–5	0.5	1–50
13	3	5	5	15	500	10	75	5	0.025	1–50	0.083	1–1000
12	3	5	5	15	500	20	40	0.1	0.007	1–10	0.065	1–1000
14	3	5	5	15	500	10	75	5	0.1	0–100	1	2–20
15	0–3	0–20	5	15	500	10	75	5	0.1	0–100	1	2–20
16	0	5	5	15	500	10	75	5	0.025	0–15	1	2–50

terms with sigmoid functions are exponentially suppressed. Neglecting these, we see that only the first terms on the right-hand side of Eqs. (C3) and (C4) remain. This implies the stability of the fixed point. For large g_C and g_V, however, we cannot ignore the terms proportional to σ', which destabilize the phase-separated fixed point.

APPENDIX D: QUASIPERIODIC PHASE DIAGRAMS

We consider the case $g_C = 0$ and $g_V > 0$, where the quasiperiodic phase diagram can emerge. Following Sec. III A by assuming activity phase separation to n_h neurons with V_h and C_h and to n_l neurons with V_l and C_l, we write equations for the fixed point

$$V_h - V_{\rm eq} = \Delta V(C_h)\tau_V[(n_h - 1)r(V_h) + n_l r(V_l)], \quad \text{(D1)}$$

$$C_h - C_{\rm eq} = \Delta C\tau_C[(n_h - 1)r(V_h) + n_l r(V_l)] \quad \text{(D2)}$$

and

$$V_l - V_{\rm eq} = \Delta V(C_l)\tau_V[(n_l - 1)r(V_l) + n_h r(V_h)], \quad \text{(D3)}$$

$$C_l - C_{\rm eq} = \Delta C\tau_C[(n_l - 1)r(V_l) + n_h r(V_h)]. \quad \text{(D4)}$$

In the case where $g_C = 0$, we have $\Delta V(C_l) = 0$ and $\Delta V(C_h) = \Delta V_{\rm max}$ (for $C_h < C^*$ and $C_l > C^*$). Then, as in Sec. III A, we obtain the number of neurons firing at a low rate

$$n_l = \left\lfloor \frac{[Nr(V_h) - r(V_l)]\Delta C\tau_C + C_{\rm eq} - C^*}{\Delta C\tau_C[r(V_h) - r(V_l)]} \right\rfloor \quad \text{(D5)}$$

and simplify the equations for the somatic potentials to get $V_l = V_{\rm eq}$ and

$$\frac{V_h - V_{\rm eq}}{\Delta V_{\rm max}\tau_V} = Nr(V_l) - r(V_h) + \left\lceil \frac{\frac{C^*}{\Delta C\tau_C} - (N-1)r(V_l)}{r(V_h) - r(V_l)} \right\rceil, \quad \text{(D6)}$$

where the ceiling function $\lceil x \rceil$ is the smallest integer that is larger than or equal to x.

Equation (D6) does not have a solution for V_h for some parameters. Due to the ceiling function on the right-hand side, the changes happen when its argument is incremented by one, which causes the quasiperiodic structure of the phase diagram (see Fig. 16).

APPENDIX E: SIMULATION DETAILS

The code is published in [22]. We use the parameters for all figures from Table II.

[1] C. Koch, *Biophysics of Computation: Information Processing in Single Neurons* (Oxford University Press, New York, 2004).

[2] J. L. Feldman and C. A. Del Negro, Nat. Rev. Neurosci. **7**, 232 (2006).

[3] D. J. Schwab, R. F. Bruinsma, J. L. Feldman, and A. J. Levine, Phys. Rev. E **82**, 051911 (2010).

[4] J. C. Smith, H. H. Ellenberger, K. Ballanyi, D. W. Richter, and J. L. Feldman, Science **254**, 726 (1991).

[5] *Bursting: The Genesis of Rhythm in the Nervous System*, edited by S. Coombes and P. Bressloff (World Scientific, Singapore, 2005).

[6] C. A. D. Negro, C. Morgado-Valle, and J. L. Feldman, Neuron **34**, 821 (2002).
[7] C. Morgado-Valle, L. Beltran-Parrazal, M. DiFranco, J. L. Vergara, and J. L. Feldman, Am. J. Physiol. **586**, 4531 (2008).
[8] S. N. Dorogovtsev, A. V. Goltsev, and J. F. F. Mendes, Phys. Rev. Lett. **96**, 040601 (2006).
[9] T. Nishikawa and A. E. Motter, Phys. Rev. Lett. **117**, 114101 (2016).
[10] J. C. Rekling, X. M. Shao, and J. L. Feldman, J. Neurosci. **20**, RC113 (2000).
[11] S. Ashhad and J. L. Feldman, Neuron **106**, 482 (2020).
[12] P. A. Gray, W. A. Janczewski, N. Mellen, D. R. McCrimmon, and J. L. Feldman, Nat. Neurosci. **4**, 927 (2001).
[13] P. Erdös and A. Rényi, Publ. Math. Debrecen **6**, 290 (1959).
[14] T. Mizuguchi and M. Sano, Phys. Rev. Lett. **75**, 966 (1995).
[15] H. Sakaguchi, Phys. Rev. E **64**, 047101 (2001).
[16] S. H. Strogatz, *Nonlinear Dynamics and Chaos: With Applications to Physics, Biology, Chemistry and Engineering* (Westview, Boulder, 2000).
[17] F. A. Lucini, G. D. Ferraro, M. Sigman, and H. A. Makse, Neuroscience **411**, 280 (2019).
[18] F. Morone, G. Del Ferraro, and H. A. Makse, Nat. Phys. **15**, 95 (2019).
[19] G. D. Bader and C. W. Hogue, BMC Bioinf. **4**, 2 (2003).
[20] S. B. Seidman, Soc. Netw. **5**, 269 (1983).
[21] N. Lahav, B. Ksherim, E. Ben-Simon, A. Maron-Katz, R. Cohen, and S. Havlin, New J. Phys. **18**, 083013 (2016).
[22] https://github.com/mbibireata/Networks.